Available online at www.sciencedirect.com
ScienceDirect
Ceramics International 38 (2012) 311–316
CERAMICS INTERNATIONAL
www.elsevier.com/locate/ceramint

Properties and rapid consolidation of nanostructured $MgO–MgAl_2O_4$ composites

In-Jin Shon [a,*], In-Yong Ko [a], Hyun-Su Kang [a], Kyung-Tae Hong [b], Jung-Mann Doh [b], Jin-Kook Yoon [b]

[a] *Division of Advanced Materials Engineering and the Research Center of Advanced Materials Development, Engineering College, Chonbuk National University, 561-756, Republic of Korea*
[b] *Advanced Functional Materials Research Center, Korea Institute of Science and Technology, PO Box 131, Cheongryang, Seoul 130-650, Republic of Korea*

Received 18 April 2011; received in revised form 4 July 2011; accepted 5 July 2011
Available online 18th July 2011

Abstract

The rapid sintering of nanostructured $MgO–MgAl_2O_4$ composites was investigated with a high-frequency induction heated sintering process. The advantage of this process is that it allows for very quick densification to near theoretical density and prohibits grain growth in nanostructured materials. Highly dense nanostructured $MgO–MgAl_2O_4$ composites were produced with simultaneous application of 80 MPa pressure and an induced output current of total power capacity (15 kW) within 2 min. The sintering behaviors, grain sizes and mechanical properties of $MgO–MgAl_2O_4$ composites were investigated.

Keywords: B. Composite; C. Mechanical properties; Nanostuctures; Microstructure

1. Introduction

MgO is widely used in the steel industry or in non-ferrous metallurgical applications under severe conditions [1]. The lifespan of MgO is curtailed by a combinatory attack of corrosion and mechanical erosion. Refractory wear is very often the strongest at the interface of the melt wetted lining areas [2]. To improve wear properties, the addition of a second phase to form composites and nanostructured materials is common. One example is the addition of $MgAl_2O_4$ to MgO to improve the properties of the MgO. The attractive properties of $MgAl_2O_4$ are a high hardness (16 GPa), low density (3.58 g/cm^3), high melting point (2135 °C), high chemical inertness and high thermal shock resistance [3–6].

Nanocrystalline materials have received much attention as advanced engineering materials with improved physical and mechanical properties [7,8]. Attention has been directed to the application of nanomaterials as they possess high strength, high hardness, excellent ductility and toughness [9,10]. Recently, nanocrystalline powders have been developed using the thermochemical and thermomechanical processes of the spray conversion process (SCP), co-precipitation and high-energy milling [11–13]. However, grain sizes in sintered materials are greater than those in pre-sintered powders due to fast grain growth during the conventional sintering process. Therefore, even though the initial particle size is less than 100 nm, the grain size increases rapidly up to 2 μm or greater during conventional sintering [14]. As a result, controlling the grain growth during sintering is one of the keys to the commercial success of nanostructured materials. High frequency induction heated sintering (HFIHS), which can produce dense materials within 2 min, has been shown to be effective for achieving this goal [15].

In this study, the sintering of $MgO–MgAl_2O_4$ composites was investigated using the HFIHS method. The goal of this research is to produce dense nanostructured $MgO–MgAl_2O_4$ composites. In addition, the effects of $MgAl_2O_4$ on the mechanical properties of $MgO–MgAl_2O_4$ composites were also studied.

* Corresponding author. Tel.: +82 63 270 2381; fax: +82 63 270 2386.
E-mail address: ijshon@chonbuk.ac.kr (I.-J. Shon).

0272-8842/$36.00
doi:10.1016/j.ceramint.2011.07.008

2. Experimental procedure

The MgO powder with a grain size <1 μm and 99% purity and Al_2O_3 powder with a grain size of <2.2 μm and 99.99% purity used in this research were supplied by Alfa. The powders (MgO–10 wt% Al_2O_3, MgO–20 wt% Al_2O_3, MgO–30 wt% Al_2O_3, MgO–40 wt% Al_2O_3, and MgO–50 wt% Al_2O_3) were first milled in a high-energy ball mill (Pulverisette-5 planetary mill) at 250 rpm for 4 h. Tungsten carbide balls (9 mm in diameter) were used in a sealed cylindrical stainless steel vial under an argon atmosphere at a ball-to-powder weight ratio of 30:1.

The powders were placed in a graphite die (outside diameter, 45 mm; inside diameter, 20 mm; height, 40 mm) and introduced into the HFIHS apparatus shown schematically in Ref. [15]. The HFIHS apparatus included a 15 kW power supply that provided an induced current through the sample and a 50 kN uniaxial press. The system was first evacuated and a uniaxial pressure of 80 MPa was applied. An induced current was then activated and maintained until the densification rate was negligible, as indicated by real-time output of the shrinkage of

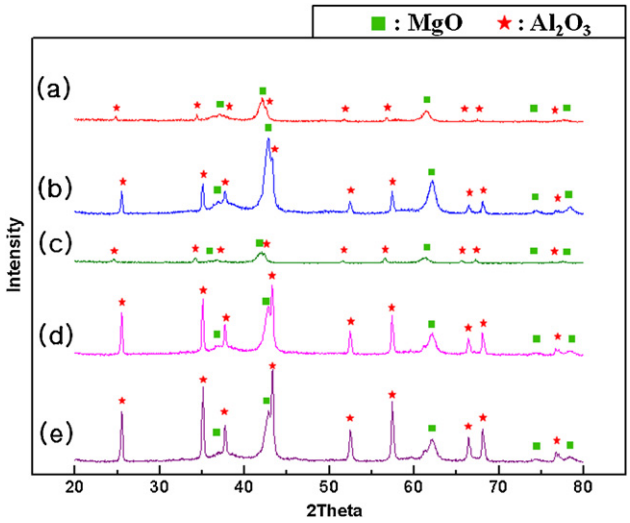

Fig. 1. X-ray diffraction patterns of the powders milled for 4 h; (a) MgO–10 wt% Al_2O_3, (b) MgO–20 wt Al_2O_3, (c) MgO–30 wt% Al_2O_3, (d) MgO–40 wt% Al_2O_3, and (e) MgO–50 wt% Al_2O_3.

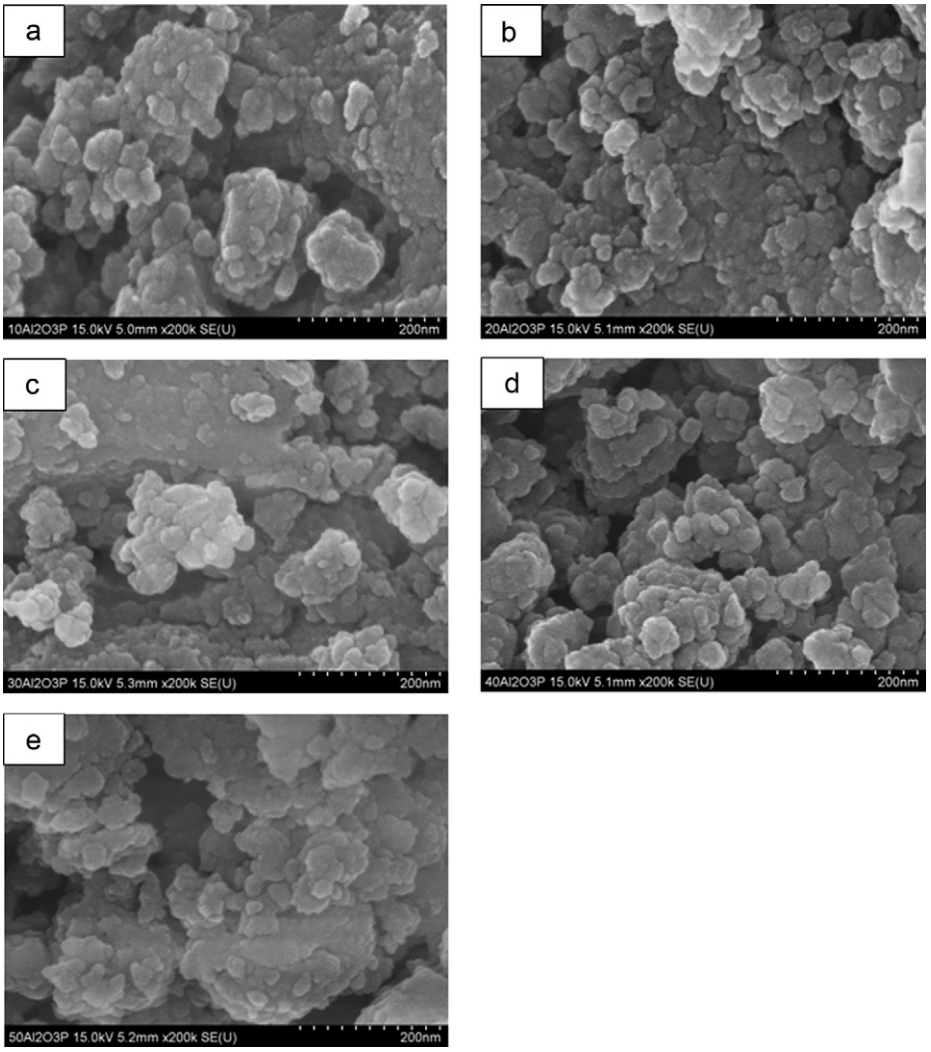

Fig. 2. FE-SEM images of the powders milled for 4 h; (a) MgO–10 wt% Al_2O_3, (b) MgO–20 wt Al_2O_3, (c) MgO–30 wt% Al_2O_3, (d) MgO–40 wt% Al_2O_3, and (e) MgO–50 wt% Al_2O_3.

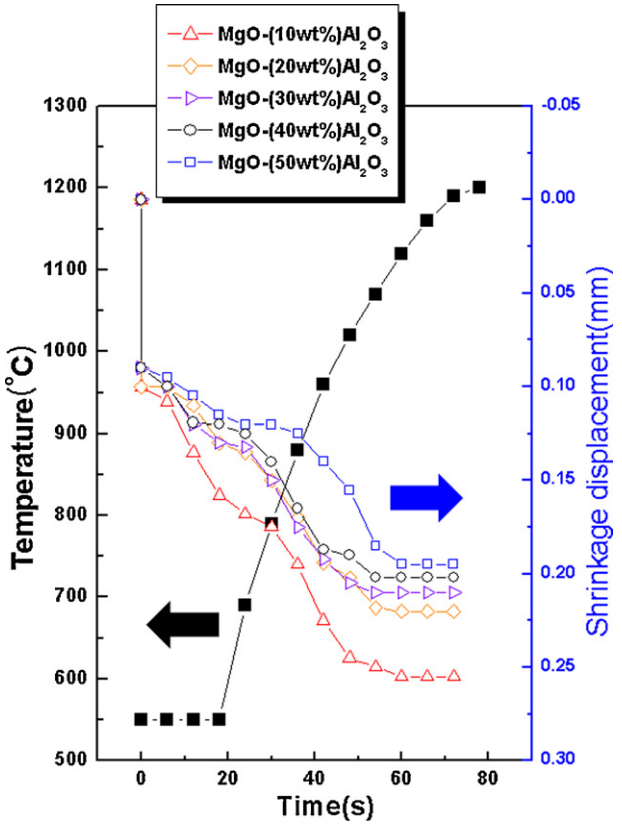

Fig. 3. Variations in temperature and shrinkage with heating time during the sintering of MgO and Al_2O_3 powders milled for 4 h.

the sample. The shrinkage was measured by a linear gauge, which detected the vertical displacement. The HFIHS can be controlled by temperature or output control, and the latter was chosen to investigate the effect of the total power output, given that the induced current level had a direct effect on the rate of heating and on the maximum temperature. The output level in this study was 80% of the total power. Temperatures were measured using a pyrometer focused on the surface of the graphite die. At the completion of the process, the induced current was turned off and the sample was cooled to room temperature. The process was performed under vacuum at 5.33 Pa.

The relative density of the sintered sample was measured using the Archimedes method. Microstructural information was obtained from product samples, which had been polished and thermally etched for 1 h at 1100 °C. Compositional and microstructural analyses of the products were conducted through X-ray diffraction (XRD) and field emission scanning electron microscopy (FE-SEM) with energy dispersive spectroscopy (EDS). Vickers hardness was measured at a load of 5 kg and a dwell time of 15 s.

3. Results and discussion

Fig. 1 shows X-ray diffraction patterns of the MgO–10 wt% Al_2O_3, MgO–20 wt% Al_2O_3, MgO–30 wt% Al_2O_3, MgO–40 wt% Al_2O_3, and MgO–50 wt% Al_2O_3 powders after high-energy ball milling for 4 h. Only MgO and Al_2O_3 peaks were detected. FE-SEM images of MgO–10 wt% Al_2O_3, MgO–20 wt% Al_2O_3, MgO–30 wt% Al_2O_3, MgO–40 wt% Al_2O_3, and MgO–50 wt% Al_2O_3 powders after milling for 4 h are shown in Fig. 2. The Al_2O_3 and MgO powders were round nanograins with milling and agglomeration. The variations in shrinkage displacement and temperature with heating time for 80% of the total output power capacity (15 kW) during the sintering of the high energy ball milled MgO–10 wt% Al_2O_3, MgO–20 wt% Al_2O_3, MgO–30 wt% Al_2O_3, MgO–40 wt% Al_2O_3 and MgO–50 wt% Al_2O_3 powders under a pressure of 80 MPa are shown in Fig. 3. In all cases, the application of the induced current resulted in shrinkage due to consolidation. The longer the induced current was applied, the more the specimens shrunk. High-energy ball milling treatment allows for the control of compound formation through fixation of the Al_2O_3 and MgO powder microstructures. Indeed, high-energy ball milling produced finer crystallites, strains and defects. Therefore, the consolidation temperature decreased due to milling because the driving force for sintering and the powder contact points for atomic diffusion increased. Fig. 4 shows the XRD patterns of specimens sintered from the high energy ball milled MgO–10 wt% Al_2O_3, MgO–20 wt% Al_2O_3, MgO–30 wt% Al_2O_3, MgO–40 wt% Al_2O_3, and MgO–50 wt% Al_2O_3 powders. The interaction between these phases, i.e.,

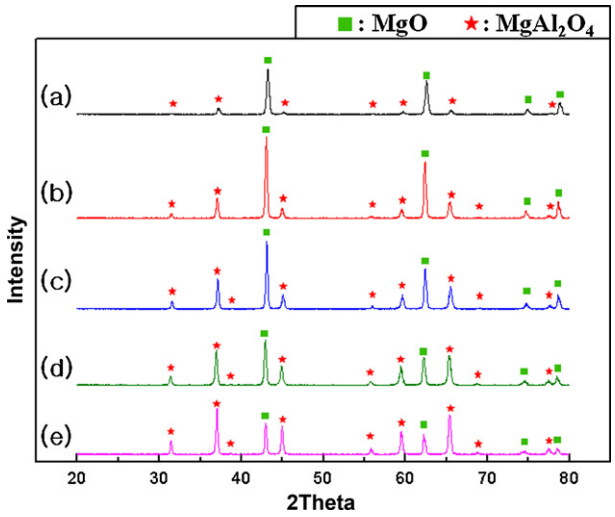

Fig. 4. X-ray diffraction patterns of the MgO–$MgAl_2O_4$ composites sintered from milled powders; (a) MgO–10 wt% Al_2O_3, (b) MgO–20 wt% Al_2O_3, (c) MgO–30 wt% Al_2O_3, (d) MgO–40 wt% Al_2O_3, and (e) MgO–50 wt% Al_2O_3.

$$Al_2O_3 + MgO \rightarrow + MgAl_2O_4 \quad (1)$$

is thermodynamically feasible [16]. FE-SEM images of MgO–$MgAl_2O_4$ composites sintered from MgO–10 wt% Al_2O_3, MgO–20 wt% Al_2O_3, MgO–30 wt% Al_2O_3, MgO–40 wt% Al_2O_3, and MgO–50 wt% Al_2O_3 powders milled for 4 h are shown in Fig. 5. The average grain sizes of MgO and $MgAl_2O_4$ in MgO–10 wt% Al_2O_3, MgO–20 wt% Al_2O_3, MgO–30 wt% Al_2O_3, MgO–40 wt% Al_2O_3 systems were approximately 500 nm, and the average grain sizes of MgO and $MgAl_2O_4$ in the MgO–10 wt% Al_2O_3 system were approximately

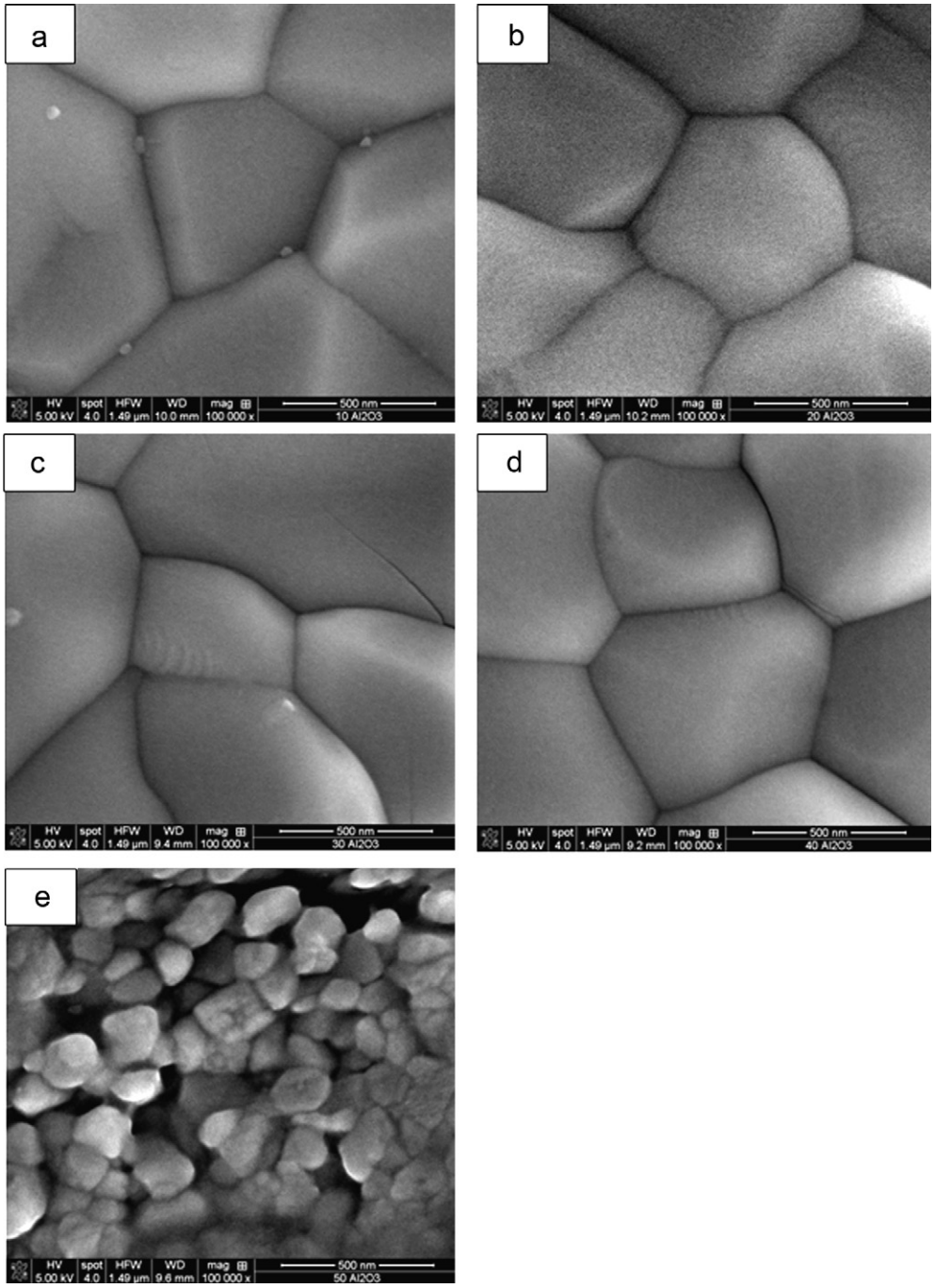

Fig. 5. FE-SEM images of the MgO–$MgAl_2O_4$ composites sintered from milled powders; (a) MgO–10 wt% Al_2O_3, (b) MgO–20 wt Al_2O_3, (c) MgO–30 wt% Al_2O_3, (d) MgO–40 wt% Al_2O_3, and (e) MgO–50 wt% Al_2O_3.

100 nm. The refinements of MgO and $MgAl_2O_4$ in the MgO–10 wt% Al_2O_3 system were due to the pinning effects of MgO and $MgAl_2O_4$, respectively.

The role of current (resistive or inductive) in sintering or synthesis processes has been the focus of several attempts to provide an explanation to the observed enhancement of sintering and the improved characteristics of the products. The role played by the current has been variously interpreted, with the effect explained in terms of a fast heating rate due to Joule heating, the presence of plasma in pores separating powder particles, and the intrinsic contribution of the current to mass transport [17–20]. The differences between SPS and HFIHS are that the specimen and die are heated by pulsed current in SPS and by induced current in HFIHS.

Vickers hardness measurements were performed on polished sections of the MgO and $MgAl_2O_4$ composites using a 5 kg load and a 15 s dwell time. Fig. 6 shows Vickers indentations in the MgO–$MgAl_2O_4$ composites sintered from MgO–10 wt% Al_2O_3, MgO–20 wt% Al_2O_3, MgO–30 wt% Al_2O_3, MgO–40 wt% Al_2O_3, and MgO–50 wt% Al_2O_3 powders. Additional

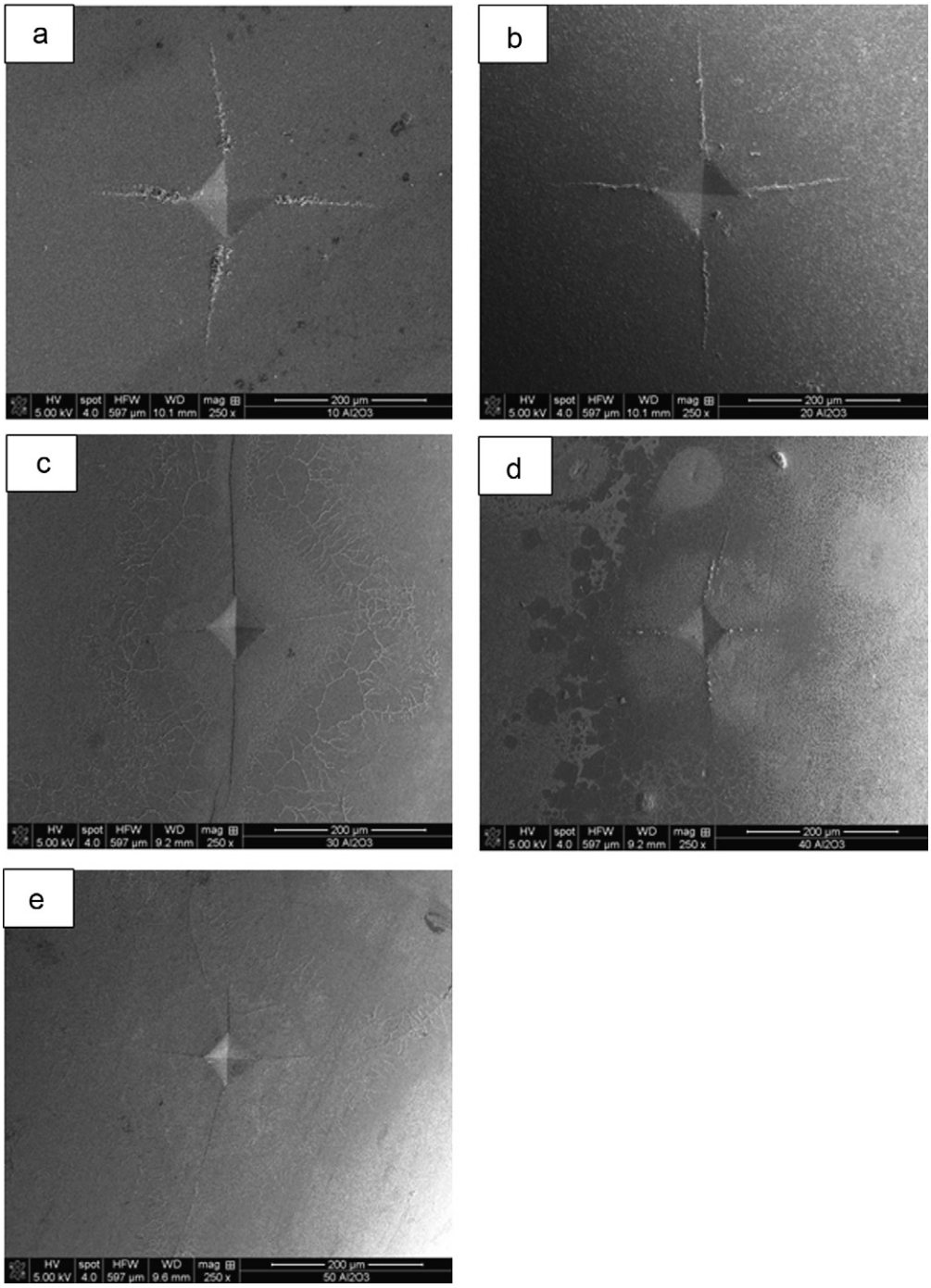

Fig. 6. Vickers indentations in the MgO–$MgAl_2O_4$ composites sintered from milled powders; (a) MgO–10 wt% Al_2O_3, (b) MgO–20 wt% Al_2O_3, (c) MgO–30 wt% Al_2O_3, (d) MgO–40 wt% Al_2O_3, and (e) MgO–50 wt% Al_2O_3.

cracks (1–3) stemming from the indentation area were observed. The Vickers hardnesses of MgO and $MgAl_2O_4$ composites sintered from MgO–10 wt% Al_2O_3, MgO–20 wt% Al_2O_3, MgO–30 wt% Al_2O_3, MgO–40 wt% Al_2O_3, and MgO–50 wt% Al_2O_3 powders milled for 4 h were 583, 638, 958, 1073, and 1277 kg/mm^2, respectively. The hardness of MgO–$MgAl_2O_4$ composites increased with an increase in $MgAl_2O_4$ content because the hardness of $MgAl_2O_4$ is greater than that of MgO.

Indentations with sufficiently large loads produced median cracks near the indent. The lengths of these cracks allow for the estimation of the fracture toughness of the materials [21]:

$$K_{IC} = 0.204\left(\frac{c}{a}\right)^{3/2} H_v a^{1/2} \quad (2)$$

where c is the length of the crack measured from the center of the indentation, a is one-half of the average length of the two indent diagonals, and H_v is the hardness. The calculated

fracture toughness for the $MgO–MgAl_2O_4$ composites sintered from MgO–10 wt% Al_2O_3, MgO–20 wt% Al_2O_3, MgO–30 wt% Al_2O_3, MgO–40 wt% Al_2O_3, and MgO–50 wt% Al_2O_3 powders were all 3 ± 0.3 MPa $m^{1/2}$. It is considered that all the K_{IC} obtained $MgO–MgAl_2O_4$ composites are about 3 MPa $m^{1/2}$ because cracks can be blocked by MgO and $MgAl_2O_4$, respectively.

4. Conclusions

Using the new rapid sintering method of HFIHS, the densification of nanostructured $MgO–MgAl_2O_4$ composites was accomplished using high energy ball milling. The Vickers hardnesses of MgO and $MgAl_2O_4$ composites sintered from MgO–10 wt% Al_2O_3, MgO–20 wt% Al_2O_3, MgO–30 wt% Al_2O_3, MgO–40 wt% Al_2O_3, and MgO–50 wt% Al_2O_3 powders milled for 4 h were 583, 638, 958, 1073, and 1277 kg/mm^2, respectively. The hardnesses of the $MgO–MgAl_2O_4$ composites increased with an increase in $MgAl_2O_4$ content without a decrease in fracture toughness.

Acknowledgment

We are grateful for the financial support from the Korea Institute of Science and Technology, which was provided through the program for study on Development of Interfacial Engineering Technology Based Plasma.

References

[1] R.K. Sauerbrey, G. Mori., Ch. Majcenovic, H. Harmuth, Corrosion protection of MgO electrodes at 1400 °C, Corros. Sci. 51 (2009) 1–5.
[2] L.B. Khoroshavin, V.B. Shcherbatskii, An electronic technology for refractories based on the periodic law, Refract. Ind. Ceram. 46 (5) (2005) 344–351.
[3] S. Anappan, L.J. Berchmans, C.O. Augustin, Sintering behavior of $MgAl_2O_4$ – a prospective anode material, Mater. Lett. 58 (2004) 2283–2289.
[4] C. Baudin, R. Martinez, P. Pena, High-temperature mechanical behavior of stoichiometric magnesium spinel, J. Am. Ceram. Soc. 78 (7) (1995) 1857–1862.
[5] P. Hing, Fabrication of translucent magnesium aluminate apinel and its compatibility in sodium vapor, J. Mater. Sci. 11 (1976) 1919–1926.
[6] J.H. Belding, E.A. Letzgus, Process for producing magnesium aluminate spinel, U.S. Patent No. 3,950,504 (April 13, 1976).
[7] M. Sherif El-Eskandarany, Structure and properties of nanocrystalline TiC full-density bulk alloy consolidation from mechanically reacted powders, J. Alloys Compd. 305 (2000) 225–238.
[8] L. Fu, L.H. Cao, Y.S. Fan, Two-step synthesis of nanostuctured tungsten carbide-cobalt powders, Scripta Mater. 44 (2001) 1061–1068.
[9] K. Niihara, A. Nikahira, Advanced Structural Inorganic Composite, Elsevier Scientific Publishing Co., Trieste, Italy, 1990.
[10] S. Berger, R. Porat, R. Rosen, Nanocrystalline materials: a study of WC-based hard metals, Prog. Mater. 42 (1997) 311–320.
[11] Z. Fang, J.W. Eason, Study of nanostuctured WC–Co composites, Int. J. Refract. Met. Hard Mater. 13 (1995) 297–303.
[12] A.I.Y. Tok, L.H. Luo, F.Y.C. Boey, Carbonate co-precipitation of Gd_2O_3-doped CeO_2 solid solution nano-particles, Mater. Sci. Eng. A 383 (2004) 229–234.
[13] I.J. Shon, D.K. Kim, I.Y. Ko, J.K. Yoon, K.T. Hong, Fabrication of nanocrystalline $TaSi_2$ composite by high frequency induction heated combustion synthesis and its mechanical properties, Mater. Sci. Forum 534-536 (2007) 525–528.
[14] J. Jung, S. Kang, Sintered (Ti,W)C carbides, Scripta Mater. 56 (2007) 561–564.
[15] H.C. Kim, I.J. Shon, Z.A. Munir, Rapid sintering of ultra-fine WC–10wt% Co by high-frequency induction heating, J. Mater. Sci. 40 (2005) 2849–2854.
[16] O. Knacke, O. Kubaschewski, K. Hesselmann, Thermochemical Properties of Inorganic Substances, Springer-Verlag, 1991.
[17] Z. Shen, M. Johnsson, Z. Zhao, M. Nygren, Spark plasma sintering of alumina, J. Am. Ceram. Soc. 85 (2002) 1921–1927.
[18] J.E. Garay, U. Anselmi-Tamburini, Z.A. Munir, S.C. Glade, P. Asoka-Kumar, Electric current enhanced defect mobility in Ni_3Ti intermetallic electric current enhanced defect mobility in Ni_3Ti intermetallics, Appl. Phys. Lett. 85 (2004) 573–575.
[19] J.R. Friedman, J.E. Garay, U. Anselmi-Tamburini, Z.A. Munir, Modified interfacial reactions in Ag–Zn multilayers under the influence of high DC currents, Intermetallics 12 (2004) 589–597.
[20] J.E. Garay, J.E. Garay, U. Anselmi-Tamburini, Z.A. Munir, Enhanced growth of intermetallic phases in the Ni–Ti system by current effects, Acta Mater. 51 (2003) 4487–4495.
[21] K. Niihara, R. Morena, D.P.H. Hasselman, Evaluation of KIC of brittle solids by the indentation method with low crack-to-indent ratios, J. Mater. Sci. Lett. 1 (1982) 12–16.